Article

Prussian Blue Analogues Derived Penroseite (Ni,Co)Se2 Nanocages Anchored on 3D Graphene Aerogel for Efficient Water Splitting

Xun Xu, Hanfeng Liang, Fangwang Ming, Zhengbing Qi, Yaqiang Xie, and Zhoucheng Wang

Just Accepted

Prussian Blue Analogues Derived Penroseite

(Ni,Co)Se$_2$ Nanocages Anchored on 3D Graphene

Aerogel for Efficient Water Splitting

Xun Xu,[†] Hanfeng Liang,[‡,] Fangwang Ming,[†] Zhengbing Qi,[#] Yaqiang Xie,[†] and Zhoucheng Wang[†,*]*

[†]College of Chemistry and Chemical Engineering, Xiamen University, Xiamen 361005, China;

[‡]Materials Science and Engineering, King Abdullah University of Science and Technology (KAUST), Thuwal 23955-6900, Saudi Arabia; [#]College of Materials Science and Engineering, Xiamen University of Technology, Xiamen 361024, China

ABSTRACT: Efficient water splitting demands highly active, low cost, and robust electrocatalysts. In this study, we report the synthesis of penroseite (Ni,Co)Se$_2$ nanocages anchored on 3D graphene aerogel using Prussian blue analogues as precursor and further their applications in overall water splitting electrolysis. The synergy between the high activity of (Ni,Co)Se$_2$ and the good conductivity of graphene leads to superior performance of the hybrid toward the water splitting in basic solutions. The (Ni,Co)Se$_2$-GA only requires a low cell voltage of 1.60 V to reach the current density of 10 mA cm^{-2}, making the (Ni,Co)Se$_2$-GA hybrid a competitive alternative to noble metal based catalysts for water splitting.

Hydrogen energy is a green and renewable fuel that has the potential to replace fossil fuels in the future.[1,2] Water splitting driven by electricity (ideally by solar energy) is one of the most promising ways to produce hydrogen with high purity. Efficient water splitting demands highly active and robust catalysts that can substantially expedite the sluggish kinetics of the two half reactions, namely the oxygen evolution reaction (OER) and the hydrogen evolution reaction (HER).[3-6] Noble metal based compounds such as Pt, RuO$_2$, and IrO$_2$ are currently state-of-the-art catalysts, while their large-scale applications are greatly limited by the high cost and scarcity. Consequently, tremendous efforts have been devoted toward exploring non-noble metal-based electrocatalysts (e.g., oxides, hydroxides, and phosphates for OER, whereas chalcogenides, carbides, and phosphides for HER), especially those can effectively catalyze both the OER and HER.[3-25] Among them, earth abundant transition metal selenides have attracted considerable attention due to their low cost and high activity. These compounds were firstly found to be highly active for HER, and have lately shown their efficacy for OER though the real active materials are the surface (oxy)hydroxides in situ formed under OER conditions.[26] Notably, pyrite CoSe$_2$ has become a promising candidate because of its electronic configuration ($t_{2g}^6 e_g^1$, strong Jahn-Teller effect) that is close to the optimal e_g filling for OER.[27] Many strategies have been proposed to further enhance the electrocatalytic performance of CoSe$_2$, for example, by delicately nanostructuring (e.g., ultrathin nanoplates) to expose more active sites,[28] by constructing hybrid structures (e.g., Mn$_3$O$_4$/CoSe$_2$) to utilize the synergistic effect,[29] or by doping (e.g., Ag-CoSe$_2$) to enhance the conductivity.[30] We noticed that the Ni-doped Co$_{0.85}$Se

can significantly improve the electrical conductivity, and thus the OER activity.[26] In addition, we have previsouly demonstrated that Co-doped $NiSe_2/Ni_3Se_4$ exhibit good electrocatalytic activity for both the HER and OER.[14] The coexistence of heterogeneous spin states, namely Ni and Co atoms, could lead to lattice distortion and subtle atomic arrangement because of the mismatch in Jahn-Teller distortion degree (Ni^{2+}, $t_{2g}^6 e_g^2$, both t_{2g} and e_g orbitals are evenly occupied, resulting no Jahn-Teller effect).[14] Such arrangement can provide additional active edge sites as demonstrated previsouly in the case of Mn-doped $CoSe_2$.[31] In these studies, however, the amounts of the dopants are often very low (for example, the atomic ratio of Co:Ni in Co-doped $NiSe_2/Ni_3Se_4$ is only 0.03:1), which means the main composition of these materials is still monometallic selenides. Bimetallic compounds, on the other hand, have been shown to exhibit enhanced electrochemical properties compared to their single metal counterparts. For example, NiCoP shows superior electrochemical performance than Ni_2P and CoP.[32] Further, a synergistic effect between Ni and Co could also boost the OER performance as already confirmed for bimetallic NiCo oxides/hydroxides,[7, 12] $NiCo_2S_4$,[33] and NiCoP.[16] Meanwhile, Ni and Co based selenides have also been demonstrated to be efficient HER catalysts.[11, 15, 34-37] In view of these, bimetallic penroseite $(Ni,Co)Se_2$ should be a promising electrocatalyst for both the OER (note the real active species are surface hydroxides as will be demonstrated later) and HER. Unexpectedly, however, this specific compound has rarely been explored for electrocatalysis even though the penroseite mineral was discovered in 1925.[38]

While $(Ni,Co)Se_2$ is expected to exhibit good intrinsic catalytic activity, proper nanostructure is also of key importance to achieve optimal performance. Hollow and porous nanostructures with large surface area and abundant active sites have attracted much attention due to the enhanced performance compared to that of their solid counterparts.[11, 39] In this content, Prussian blue analogues (PBAs) with uniform sizes, various compositions, diverse morphologies and architectures can serve as ideal precursors to prepare hollow and porous

nanostructures.[40-42] Indeed, various hollow or porous nanostructured metal oxides, sulfides, and phosphides have been successfully prepared using PBAs as templates.[41, 43, 44] However, these PBAs derived materials still surfer from the structure collapse and aggregation under the severe gas evolution during the electrocatalysis. Further anchoring them into graphene could greatly improve the structural stability and the conductivity between individual particles, and therefore enhance the overall performance.

Herein we report the penroseite $(Ni,Co)Se_2$ nanocages anchored on 3D graphene aerogel (GA) synthesized from NiCo PBA precursor and further their applications in water splitting electrocatalysis. The unique morphology of nanocages provides more exposed active sites. Whereas the direct contact between $(Ni,Co)Se_2$ and reduced graphene oxide (rGO) nanosheets promotes the electron transfer. As a result, the $(Ni,Co)Se_2$-GA hybrid catalyst shows stable performance toward both the OER (note the real active species are surface hydroxides as will be demonstrated later) and HER that is superior to that of most non-noble metal based electrocatalysts reported so far. More importantly, the $(Ni,Co)Se_2$-GA can also efficiently catalyze the overall water splitting with a low voltage of 1.6 V at 10 mA cm^{-2} and outstanding durability.

The synthesis process of $(Ni,Co)Se_2$-GA hybrid (see Methods in Supporting Information for details) is illustrated in Figure 1a. NiCo PBA nanocubes (Figure 1b) were first in situ grown on graphene oxide nanosheets. The resulting NiCo PBA-GO was then subjected to a hydrothermal and consequent freeze-drying treatment to form the NiCo PBA-GA, which was then converted into $(Ni,Co)Se_2$-GA by thermal selenization at 350 ℃. The morphology of these samples was then investigated using scanning electron microscope (SEM) and transmission electron microscope (TEM). The NiCo PBA nanocubes with an edge length of ~300 nm were homogeneously anchored on graphene sheets (Figure 1c-e and Figure S1 in the Supporting Information). After selenization, the NiCo PBA-GA was converted into

(Ni,Co)Se$_2$-GA and the cubic structure was well retained (Figure 1f), though the particle size decreases to ~275 nm due to the decomposition and shrinkage during the thermal treatment. This indicates that the NiCo PBA nanocubes served as self-scarified template for the formation of (Ni,Co)Se$_2$ nanocages, which consist of numerous small nanoparticles with abundant pores (Figure 1g and h). It is noteworthy that the converted (Ni,Co)Se$_2$ nanocages are still evenly anchored on graphene sheets, suggesting the strong binding between (Ni,Co)Se$_2$ and GA. Such a geometric confinement of nanoparticles within graphene layers is expected to enhance their interfacial contact and to restrain the structure collapse and aggregation, thereby promoting the catalytic activity and stability. The high-resolution TEM (HRTEM) image (inset of Figure 1h) reveals clear fringes with interplanar spacing of 0.26 nm, corresponding to the (210) planes of (Ni,Co)Se$_2$. The energy dispersive X-ray (EDX) analysis confirms the presence of Ni, Co, and Se (Figure S2). The scanning TEM-EDX elemental maps further reveal the homogeneous distribution of Ni, Co, Se, and C elements in the hybrid. The atomic ratio of Ni and Co in the sample is 3:2 as determined by inductively coupled plasma mass spectrometry (ICP-MS, see Table S1).
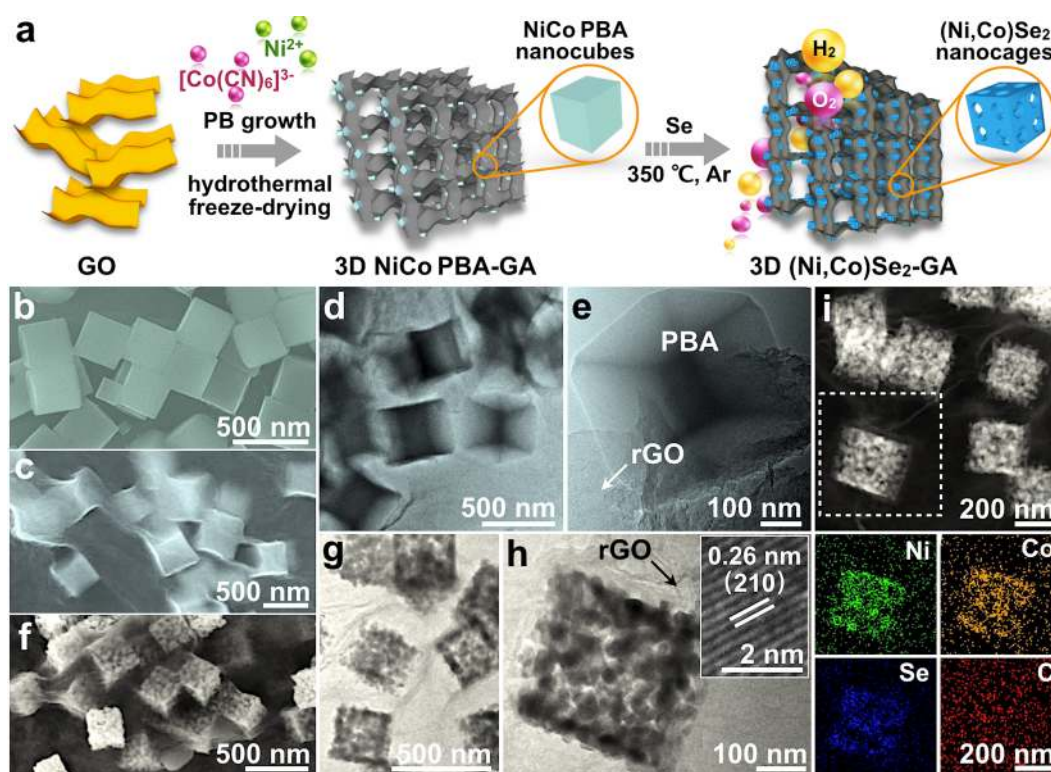
Figure 1. Morphological characterization of the (Ni,Co)Se$_2$-GA nanostructures. (a) Schematic illustration of the synthesis process of (Ni,Co)Se$_2$-GA for water splitting electrocatalysis. (b) SEM image of NiCo PBA nanocubes. (c) SEM and (d,e) TEM images of NiCo PBA-GA. (f) SEM, (g,h) TEM images, and (i) HADDF image and corresponding elemental maps of (Ni,Co)Se$_2$-GA. The inset of h shows the HRTEM image of (Ni,Co)Se$_2$-GA.

We then performed detailed structural characterization of the (Ni,Co)Se$_2$-GA samples. The X-ray diffraction (XRD) patterns (Figure 2a) suggest that the NiCo PBA (JCPDS #89-3738) was successfully converted into penroseite (Ni,Co)Se$_2$ (JCPDS #29-1417) upon thermal selenization. Both samples show a diffraction hump around 25º (2θ) that originates from the graphene network. We further performed the X-ray photoelectron spectroscopy (XPS) measurements to probe the surface composition and the oxidation state of the as-converted (Ni,Co)Se$_2$-GA. The Ni 2p core level spectrum (Figure 2b) shows two main peaks at 855.1 eV (Ni 2p$_{3/2}$) and 873.6 (Ni 2p$_{1/2}$) along with their satellite peaks, indicating the existence of Ni^{2+}.[45] The Co 2p spectrum (Figure 2c) is also splitting into 2p$_{3/2}$ and 2p$_{1/2}$ doublets due to spin-orbit

coupling. The binding energy of 780.1 eV for Co $2p_{3/2}$ and the strong shake-up peak suggest

the exist of Co^{2+}.[46] As for Se 3d, the peak at 54.7 eV can be assigned to the metal-selenium

bond, whereas the peak near 58.6 is likely related to SeO_x.[26] These results confirm the formation

of $(Ni,Co)Se_2$ on graphene.
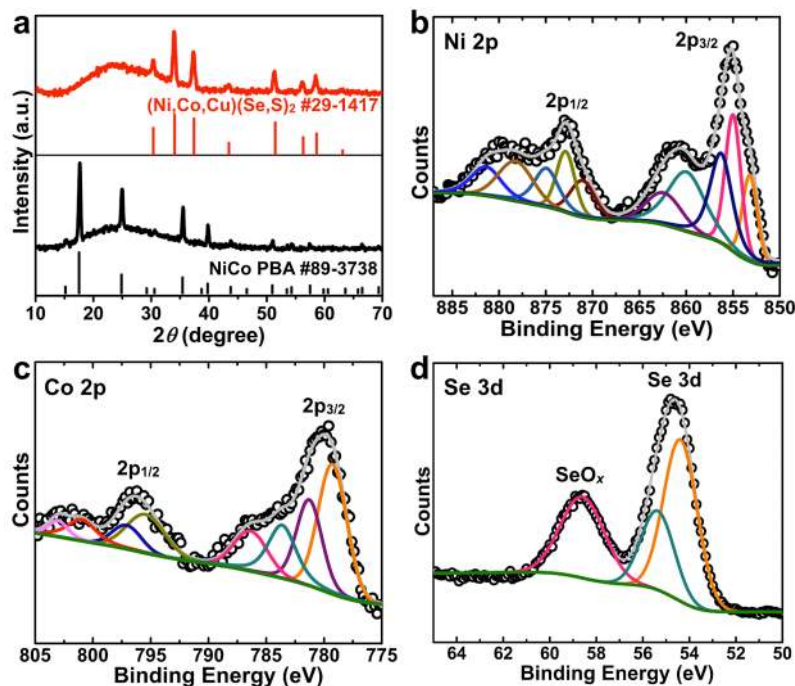
Figure 2. Structural characterization of the $(Ni,Co)Se_2$-GA nanostructures. (a) XRD patterns

of NiCo PBA-GA and $(Ni,Co)Se_2$-GA. (b) Ni 2p, (c) Co 2p, and (d) Se 3d high resolution XPS

spectra of the $(Ni,Co)Se_2$-GA.

We found that the selenization temperature has significant impacts on the phase and

structure of the final products. When the selenization temperature is below 350 ℃ (e.g., 300

℃), the NiCo PBA cannot fully convert into $(Ni,Co)Se_2$ (Figure S3) and both NiCo PBA and

$(Ni,Co)Se_2$ can be observed in the final product (Figure S4). Whereas when the temperature

raises to 300-450 ℃, $(Ni,Co)Se_2$ is successfully formed (Figure S3), however, different

nanostructures are obtained. The $(Ni,Co)Se_2$ formed at 350 ℃ shows a perfect porous cage-

like nanostructure. In contrast, only fragmentary cubic frameworks can be found in the product

obtained at 400 ℃, and the original cubic nanostructure of NiCo PBA is completely destroyed

at 450 ℃ (Figure S4). We have also varied the reaction temperature in the synthesis of NiCo PBA-GA precursors to tune the particle size of PBA nanocubes and further the converted $(Ni,Co)Se_2$ nanocages. The result shows that the particle size of PBA and thus the $(Ni,Co)Se_2$ generally becomes larger as the reaction temperature raised from 5 to 50 ℃ (Figure S5).

We first investigated the electrocatalytic OER activity of the $(Ni,Co)Se_2$-GA (formed at 350 ℃) in 1 M KOH using a standard three-electrode configuration (see Methods for details). The OER performance of $(Ni,Co)Se_2$ (see SEM image in Figure S6), GA, and RuO_2 on Ni foam were also tested for comparison. The electrodes were cycled until a stable performance was achieved (the surface of the material is likely completely oxidized into hydroxides during the first few electrochemical scans as will be discussed later). IR-corrected polarization curves were recorded at 1 mV s^{-1} (see the original data without IR correction and the Nyquist plots in Figure S7). As shown in Figure 3A, GA shows negligible current density at the potentials lower than 1.55 V vs reversible hydrogen electrode (RHE). In contrast, $(Ni,Co)Se_2$ nanocages exhibit a much higher activity with an overpotential of 320 mV to achieve the current density of 10 mA cm^{-2}. This overpotential is slightly higher (30 mV) than that of RuO_2, which is the state-of-the-art OER catalyst. The OER performance was further greatly boosted by incorporating with graphene sheets. Notably, the $(Ni,Co)Se_2$-GA electrodes only require overpotentials as low as 250 and 340 mV to drive the current density of 10 and 100 mA cm^{-2}, respectively. These overpotentials compare favorably or at least comparable to those recently reported high-performance earth-abundant OER catalysts (Table S2).[47] The anodic peak at around 1.35 V is due to the oxidation of Ni/Co species (see Figure S8 and discussion in Supporting Information). The catalytic kinetics of these catalysts were further evaluated by the Tafel slopes. The $(Ni,Co)Se_2$-GA possesses a much smaller Tafel slope of 70 mV dec^{-1}, compared to 89, 132, and 164 mV dec^{-1} for $(Ni,Co)Se_2$, RuO_2, and GA, respectively, suggesting the more favorable OER kinetics. The high OER performance of $(Ni,Co)Se_2$-GA is mainly

attributed to the high surface area and the strong coupling between $(Ni,Co)Se_2$ and GA that enhances the electrical conductivity. Compared to the direct conversion of NiCo PBA into $(Ni,Co)Se_2$ (Figure S6), anchoring NiCo PBA onto graphene sheets can greatly relieve the structural expansion during the thermal conversion, and thus prevents the aggregation of the converted $(Ni,Co)Se_2$ nanocages. As a result, the Brunauer-Emmett-Teller (BET) surface area of $(Ni,Co)Se_2$-GA (123.0 cm^2 g^{-1}) is twice as that of $(Ni,Co)Se_2$ (62.3 cm^2 g^{-1}), close to that of GA (172.8 cm^2 g^{-1}, Figure S9). The higher surface area of $(Ni,Co)Se_2$-GA would provide richer active sites and larger contact area for electrocatalytic process compared to $(Ni,Co)Se_2$. We further measured the electrochemically active surface area (ECSA) using a simple cyclic voltammetry method (Figure S10).[48] As expected, the double layer capacitance of $(Ni,Co)Se_2$-GA (16.0 mF cm^{-2}) is much higher than that of $(Ni,Co)Se_2$ (10.4 mF cm^{-2}), suggesting the $(Ni,Co)Se_2$-GA has a larger ECSA which consequently leads to a higher catalytic activity. We also compared the OER activity of the $(Ni,Co)Se_2$-GA nanostructures obtained at different selenization temperatures (300, 350, 400 and 450 ℃) and found that the $(Ni,Co)Se_2$-GA formed at 350 ℃ exhibits the optimal performance (Figure S11). The disparity in performance could be due to their different ECSAs (Figure S12). We then compared the OER activity of the $(Ni,Co)Se_2$-GA nanostructures with different particle sizes (Figure S5). The result shows that the $(Ni,Co)Se_2$ nanocages with larger particle size (by converting NiCo PBA precursor synthesized at 50 °C) exhibit inferior performance. This is understandable because big particles generally possess a low surface area. Unexpectedly, however, the $(Ni,Co)Se_2$ with smaller particle size (by converting NiCo PBA precursor synthesized at 5 °C) did not show better electrocatalytic activity, which is probably due to the lower mass loading of the material. Further, the SEM image also reveals that $(Ni,Co)Se_2$ with smaller particle size possess a nanocube but not nanocage morphology (Figure S5), which could also affect the electrocatalytic performance. We further tuned the composition of the $(Ni,Co)Se_2$-GA

nanocages and the result shows that the $(Ni,Co)Se_2$-GA (350 ºC) exhibits the best activity (Figure S13). Note that the $(Ni,Co)Se_2$-GA is much more active than $NiSe_2$-GA and $CoSe_2$-GA, suggesting the synergy between Ni and Co greatly enhances the OER activity (Figure S13). Besides the high catalytic activity, the $(Ni,Co)Se_2$-GA (350 ºC) also shows good stability as confirmed by the continuous cyclic voltammetry (CV) and the chronoamperometric measurements The CV curve recorded after 5000 CV cycles shows negligible difference compared to the initial one (Figure S14a). Moreover, the current density achieved at a static potential of 1.522 V only decrease about 6% after 20 h operation (Figure S14b), suggesting the good stability of the $(Ni,Co)Se_2$-GA catalyst. XPS measurements were conducted to probe the surface compositional change of the catalyst after the OER catalysis (Figure S15). The Se 3d XPS spectrum suggests an increase in SeO_x amount after OER, indicating the surface of the $(Ni,Co)Se_2$-GA has been oxidized upon the strong oxidative conditions during OER. Such phenomenon is commonly seen for metal selenides after OER catalysis.[26] The XPS data also indicates that there are Ni^{3+} and Co^{3+} species generated on the surface of the catalyst. Note that it has been now well established that the real active surface OER sites for metal chalcogenides[26] and phosphides[16, 49] are the surface *in situ* generated metal oxides/hydroxides due to the strong oxidative conditions during the OER. To further support this argument, we have carried out XRD and Raman characterizations on the post-OER samples (Figure S16). Even though the bulk phase does not change after the OER (which is possible since the *in situ* surface generated hydroxide/oxide layers are highly likely amorphous), the Raman spectrum of the post-OER catalyst, however, suggests the formation of Ni/Co hydroxides. The two new broad peaks at 410 and 540 cm^{-2} are associated with Co and Ni hydroxides, respectively.[50, 51] Indeed, an amorphous surface layer can be identified by the TEM imaging (Figure S17). Together with the XPS data, it is clear that the surface of the catalyst has been oxidized into hydroxides, which should be the real OER active sites. These results suggest that the $(Ni,Co)Se_2$-GA only serves

as "precatalyst" but not the real OER active species. The stable apparent performance could be because the surface oxidation to hydroxides is complete in first a few CV scans (see Figure S14a). Note that Ni foam is also active for OER, we have therefore loaded the catalyst onto carbon cloth and remeasured the OER activity (Figures S18 and S19). The result shows that the performance of $(Ni,Co)Se_2$-GA/Ni foam and $(Ni,Co)Se_2$-GA/carbon cloth are almost the same, which suggests that the main contribution for OER comes from the catalyst itself but not the substrate.
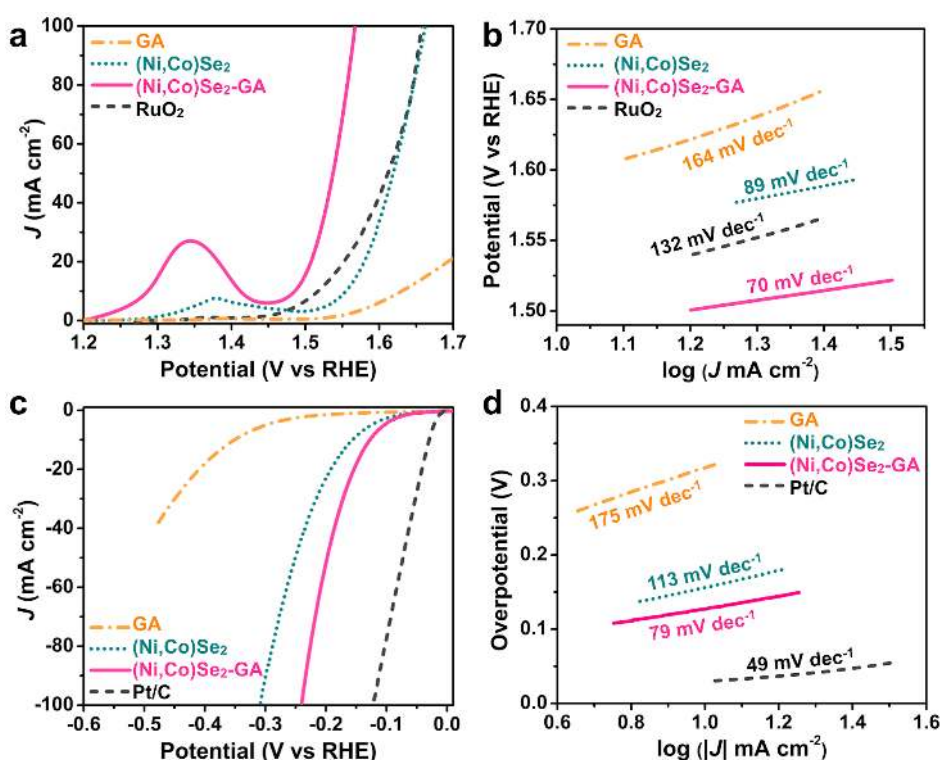

Figure 3. $(Ni,Co)Se_2$-GA loaded on Ni foam for (a,b) OER and (c,d) HER electrocatalysis in 1 M KOH along with $(Ni,Co)Se_2$, GA, and RuO_2 for comparison. (a,c) *IR*-corrected polarization curves and (b,d) the corresponding Tafel plots.

We then studied the HER performance of the $(Ni,Co)Se_2$-GA samples in 1 M KOH (see Methods for details). We first optimized the synthetic conditions and found that the $(Ni,Co)Se_2$-GA formed at 350 ℃ (using PBA synthesized at 25 ℃ as precursor) exhibits the highest HER activity (Figures S5 and S20). We further compared the HER activity of $(Ni,Co)Se_2$-GA

(synthesized at 350 ºC), (Ni,Co)Se$_2$, Pt/C, and GA on Ni foam under the same conditions. As shown in Figure 3c, the Pt/C shows the best performance followed by the (Ni,Co)Se$_2$-GA, which only needs an overpotential of 128 mV to achieve the current density of -10 mA cm^{-2}. This potential is 28 and 190 mV lower than that of (Ni,Co)Se$_2$ and GA, respectively. Furthermore, the current density can be scaled to -100 mA cm^{-2} at overpotential of 240 mV for (Ni,Co)Se$_2$-GA. These potentials compare favorably to that reported for metal chalcogenides and other earth-abundant HER catalysts in basic or even in acidic electrolytes (Table S3).[52] For example, the overpotential at -10 mA cm^{-2} is much lower than that for Ni$_3$Se$_2$ nanoforest on Ni foam in 1 M NaOH (203 mV),[53] and CoS$_2$ in 0.5 M H$_2$SO$_4$ (145 mV).[48] The high activity of the (Ni,Co)Se$_2$-GA is also confirmed by its relatively small Tafel slope of 79 mV dec^{-1}, compared to 113 and 175 mV dec^{-1} of (Ni,Co)Se$_2$ and GA, respectively (Figure 3d). Similarly as we observed in OER measurements, the (Ni,Co)Se$_2$-GA also exhibits better HER performance than NiSe$_2$-GA and CoSe$_2$-GA. Besides the high activity, the (Ni,Co)Se$_2$-GA also shows good stability (Figure S21). The polarization curve barely shifts after 2000 CV cycles. Besides, the current density achieved at a given overpotential of 180 mV only a slight decrease after 20 h, suggesting the robust of the catalyst. The XPS analysis of the post-HER (Ni,Co)Se$_2$-GA reveals that the main composition remains (Ni,Co)Se$_2$ though the surface SeO$_x$ amount increases (Figure S22), which could be due to the surface oxidation of Se in strong basic solutions.[14] Whereas the XRD and Raman indicate there are no changes in bulk material after the HER measurements (Figure S16).

Water splitting catalyzed by the same material could greatly simply the water splitting system and lower the production cost. Encouraged by the impressive catalytic activity of the (Ni,Co)Se$_2$-GA toward both the OER (though the real active species is the surface hydroxides as demonstrated earlier) and HER, we then assembled a water electrolyzer employing the (Ni,Co)Se$_2$-GA as both the anode and cathode for overall water splitting in 1 M KOH. The

$(Ni,Co)Se_2\|(Ni,Co)Se_2$, GA\|GA, and Pt/C\|RuO$_2$ loaded on Ni foam were also tested for comparison. As shown in Figure 4a, the overall water splitting by GA and $(Ni,Co)Se_2$ require cell voltages of 1.85 and 1.69 V to drive 10 mA cm^{-2}, respectively. In contrast, the voltage needed for $(Ni,Co)Se_2$-GA is as low as 1.60 V. This voltage is close to that of Pt/C\|RuO$_2$ (1.56 V) and is among the lowest reported values (Table S4). Note that the $(Ni,Co)Se_2$-GA can drive high current densities (e.g., 100 mA cm^{-2}) at cell voltages that are comparable to those of Pt/C\|RuO$_2$, which is important for practical H$_2$ production and makes the $(Ni,Co)Se_2$-GA a competitive alternative for water splitting. In addition, the $(Ni,Co)Se_2$-GA also shows good durability as demonstrated by the chronopotentiometric test over 40 h (Figure 4b). The voltage only slightly increases from 1.60 to 1.61 V and 1.69 to 1.70 V to achieve 10 and 30 mA cm^{-2} after 20 h operation, respectively. The faradaic efficiency of $(Ni,Co)Se_2$-GA was calculated to be ~97% by comparing the experimental H$_2$/O$_2$ production amounts with the theoretic values (Figure 4c).
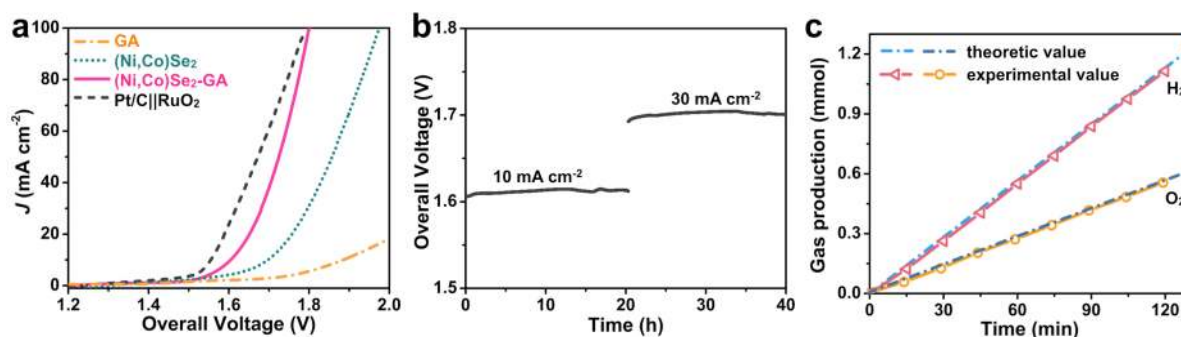

Figure 4. $(Ni,Co)Se_2$-GA for overall water splitting electrocatalysis in 1 M KOH. (a) *IR*-corrected polarization curves and (b) long-term stability tests carried out at 10 and 30 mA cm^{-2}. (c) H$_2$ and O$_2$ production catalyzed by $(Ni,Co)Se_2$-GA in 1 M KOH at room temperature. The dash lines present the theoretic value H$_2$ and O$_2$ amounts expected for a 100% Faradaic efficiency.

The high activity and excellent stability of the 3D penroseite $(Ni,Co)Se_2$-GA can be attributed to the following aspects. (I) The synergistic effect between Ni and Co could

significantly boost the catalytic performance, which is confirmed by the fact that the $NiSe_2$-GA and $CoSe_2$-GA shows inferior performance toward both the HER and OER (Figure S13). Further, the mismatch in the Jahn-Teller distortion degree of Ni and Co could result in subtle atomic arrangement, which offers more active sites. (II) The unique nanocage structure of $(Ni,Co)Se_2$ not only provides large surface area that guarantees more exposure of active sites, but also facilitates the diffusion of electrolyte and gas evolution. (III) The strong coupling between the $(Ni,Co)Se_2$ nanocages and the graphene sheets promotes the charge transport. Note that the physically mixed $(Ni,Co)Se_2$/GA catalyst is not as active as $(Ni,Co)Se_2$-GA (Figure S23), suggesting the strong bonding between $(Ni,Co)Se_2$ and GA plays an important role. (IV) The 3D graphene network with abundant open spaces effectively relieves the structure collapse of $(Ni,Co)Se_2$ during the electrocatalysis.

In summary, we have synthesized penroseite $(Ni,Co)Se_2$ nanocages using NiCo PBA as precursor and further anchored them onto graphene aerogel. The resulted $(Ni,Co)Se_2$-GA inherits the high catalytic activity of $(Ni,Co)Se_2$ and the high conductivity of the graphene sheets, and consequently exhibits superior performance toward the water splitting electrolysis. The overall current density of 10 mA cm^{-2} can be achieved at a cell voltage as low as 1.60 V on $(Ni,Co)Se_2$-GA electrodes in 1 M KOH. Our work not only establishes the $(Ni,Co)Se_2$-GA as a high performance and stable water splitting electrodes but also provides a general strategy to prepare metal selenides/graphene hybrid catalysts with well-defined nanostructures and further to greatly enhance their performance in electrocatalysis and many other applications.

ASSOCIATED CONTENT

Supporting Information. The following files are available free of charge.

Experimental details, additional supporting data, and comparison of catalytic performance, as noted in the main text (PDF)

AUTHOR INFORMATION

Corresponding Author

*E-mail: hanfeng.liang@kaust.edu.sa (H. Liang); zcwang@xmu.edu.cn (Z. Wang)

Notes

The authors declare no competing financial interest.

ACKNOWLEDGMENT

REFERENCES

(1)   Lewis, N. S.; Nocera, D. G. *Proc. Natl. Acad. Sci. U.S.A.* **2006**, *103*, 15729-15735.

(2)   Turner, J. A. *Science* **2004**, *305*, 972-974.

(3)   Jiao, Y.; Zheng, Y.; Jaroniec, M.; Qiao, S. Z. *Chem. Soc. Rev.* **2015**, *44*, 2060-2086.

(4)   Zheng, Y.; Jiao, Y.; Jaroniec, M.; Qiao, S. Z. *Angew. Chem. Int. Ed.* **2015**, *54*, 52-65.

(5)   Faber, M. S.; Jin, S. *Energy Environ. Sci.* **2014**, *7*, 3519-3542.

(6)   Hong, W. T.; Risch, M.; Stoerzinger, K. A.; Grimaud, A.; Suntivich, J.; Shao-Horn, Y. *Energy Environ. Sci.* **2015**, *8*, 1404-1427.

(7)   Gao, X.; Zhang, H.; Li, Q.; Yu, X.; Hong, Z.; Zhang, X.; Liang, C.; Lin, Z. *Angew. Chem. Int. Ed.* **2016**, *55*, 6290-6294.

(8)   Feng, J. X.; Ding, L. X.; Ye, S. H.; He, X. J.; Xu, H.; Tong, Y. X.; Li, G. R. *Adv. Mater.* **2015**, *27*, 7051-7057.

(9)   Feng, J. X.; Xu, H.; Dong, Y. T.; Ye, S. H.; Tong, Y. X.; Li, G. R. *Angew. Chem.* **2016**, *128*, 3758-3762.

(10)   Wang, A.-L.; Xu, H.; Li, G.-R. *ACS Energy Lett.* **2016**, *1*, 445-453.

(11)   Liang, H.; Li, L.; Meng, F.; Dang, L.; Zhuo, J.; Forticaux, A.; Wang, Z.; Jin, S. *Chem. Mater.* **2015**, *27*, 5702-5711.

(12)   Liang, H.; Meng, F.; Cabán-Acevedo, M.; Li, L.; Forticaux, A.; Xiu, L.; Wang, Z.; Jin, S. *Nano Lett.* **2015**, *15*, 1421-1427.

(13)   Liang, H.; Shi, H.; Zhang, D.; Ming, F.; Wang, R.; Zhuo, J.; Wang, Z. *Chem. Mater.* **2016**, *28*, 5587-5591.

(14)   Ming, F.; Liang, H.; Shi, H.; Xu, X.; Mei, G.; Wang, Z. *J. Mater. Chem. A* **2016**, *4*, 15148-15155.

(15)   Zhuo, J.; Cabán-Acevedo, M.; Liang, H.; Samad, L.; Ding, Q.; Fu, Y.; Li, M.; Jin, S. *ACS Catal.* **2015**, *5*, 6355-6361.

(16)   Liang, H.; Gandi, A. N.; Anjum, D. H.; Wang, X.; Schwingenschlögl, U.; Alshareef, H. N. *Nano Lett.* **2016**, *16*, 7718-7725.

(17)   Dutta, A.; Samantara, A. K.; Dutta, S. K.; Jena, B. K.; Pradhan, N. *ACS Energy Lett.* **2016**, *1*, 169-174.

(18)   Fu, S.; Zhu, C.; Song, J.; Engelhard, M. H.; Li, X.; Du, D.; Lin, Y. *ACS Energy Lett.* **2016**, *1*, 792-796.

(19)   Masa, J.; Barwe, S.; Andronescu, C.; Sinev, I.; Ruff, A.; Jayaramulu, K.; Elumeeva, K.; Konkena, B.; Roldan Cuenya, B.; Schuhmann, W. *ACS Energy Lett.* **2016**, *1*, 1192-1198.

(20)   Burke, M. S.; Enman, L. J.; Batchellor, A. S.; Zou, S.; Boettcher, S. W. *Chem. Mater* **2015**, *27*, 7549-7558.

(21)   Batchellor, A. S.; Boettcher, S. W. *ACS Catal*. **2015**, *5*, 6680-6689.

(22)   Trotochaud, L.; Ranney, J. K.; Williams, K. N.; Boettcher, S. W. *J. Am. Chem. Soc.* **2012**, *134*, 17253-17261.

(23)   Wang, J.; Wang, W.; Wang, Z.; Chen, J. G.; Liu, C.-j. *ACS Catal*. **2016**, *6*, 6585-6590.

(24)   Li, S.; Wang, S.; Salamone, M. M.; Robertson, A. W.; Nayak, S.; Kim, H.; Tsang, S. E.; Pasta, M.; Warner, J. H. *ACS Catal*. **2016**, *7*, 877-886.

(25)   Li, Y.; Yu, Y.; Huang, Y.; Nielsen, R. A.; Goddard III, W. A.; Li, Y.; Cao, L. *ACS Catal*. **2014**, *5*, 448-455.

(26)   Xia, C.; Jiang, Q.; Zhao, C.; Hedhili, M. N.; Alshareef, H. N. *Adv. Mater*. **2016**, *28*, 77-85.

(27)   Suntivich, J.; May, K. J.; Gasteiger, H. A.; Goodenough, J. B.; Shao-Horn, Y. *Science* **2011**, *334*, 1383-1385.

(28)   Liu, Y.; Cheng, H.; Lyu, M.; Fan, S.; Liu, Q.; Zhang, W.; Zhi, Y.; Wang, C.; Xiao, C.; Wei, S. *J. Am. Chem. Soc*. **2014**, *136*, 15670-15675.

(29)   Gao, M.-R.; Xu, Y.-F.; Jiang, J.; Zheng, Y.-R.; Yu, S.-H. *J. Am. Chem. Soc*. **2012**, *134*, 2930-2933.

(30)   Zhao, X.; Zhang, H.; Yan, Y.; Cao, J.; Li, X.; Zhou, S.; Peng, Z.; Zeng, J. *Angew. Chem. Int. Ed*. **2017**, *56*, 328-332.

(31)   Liu, Y.; Hua, X.; Xiao, C.; Zhou, T.; Huang, P.; Guo, Z.; Pan, B.; Xie, Y. *J. Am. Chem. Soc*. **2016**, *138*, 5087-5092.

(32)   Liang, H.; Xia, C.; Jiang, Q.; Gandi, A. N.; Schwingenschlögl, U.; Alshareef, H. N. *Nano Energy* **2017**, *35*, 331-340.

(33)   Sivanantham, A.; Ganesan, P.; Shanmugam, S. *Adv. Funct. Mater*. **2016**, *26*, 4661-4672.

(34)   Chen, P.; Xu, K.; Tao, S.; Zhou, T.; Tong, Y.; Ding, H.; Zhang, L.; Chu, W.; Wu, C.; Xie, Y. *Adv. Mater*. **2016**, *28*, 7527-7532.

(35)   Zhang, H.; Yang, B.; Wu, X.; Li, Z.; Lei, L.; Zhang, X. *ACS Appl. Mater. Interfaces* **2015**, *7*, 1772-1779.

(36)   Kong, D.; Wang, H.; Lu, Z.; Cui, Y. *J. Am. Chem. Soc.* **2014**, *136*, 4897-4900.

(37)   Wang, F.; Li, Y.; Shifa, T. A.; Liu, K.; Wang, F.; Wang, Z.; Xu, P.; Wang, Q.; He, J. *Angew. Chem.* **2016**, *128*, 7033-7038.

(38)   Gordon, S. G. *Proc. Acad. Nat. Sci. Philadelphia* **1925**, *77*, 317-324.

(39)   Liang, H.; Chen, W.; Wang, R.; Qi, Z.; Mi, J.; Wang, Z. *Chem. Eng. J.* **2015**, *274*, 224-230.

(40)   Wickramaratne, N. P.; Perera, V. S.; Park, B.-W.; Gao, M.; McGimpsey, G. W.; Huang, S. D.; Jaroniec, M. *Chem. Mater.* **2013**, *25*, 2803-2811.

(41)   Han, L.; Yu, X. Y.; Lou, X. W. D. *Adv. Mater.* **2016**, *28*, 4601-4605.

(42)   Yang, Y.; Wang, S.; Jiang, C.; Lu, Q.; Tang, Z.; Wang, X. *Chem. Mater.* **2016**, *28*, 2417-2423.

(43)   Hao, J.; Yang, W.; Zhang, Z.; Tang, J. *Nanoscale* **2015**, *7*, 11055-11062.

(44)   Yu, X. Y.; Yu, L.; Wu, H. B.; Lou, X. W. D. *Angew. Chem.* **2015**, *127*, 5421-5425.

(45)   Grosvenor, A. P.; Biesinger, M. C.; Smart, R. S. C.; McIntyre, N. S. *Surf. Sci.* **2006**, *600*, 1771-1779.

(46)   Biesinger, M. C.; Payne, B. P.; Grosvenor, A. P.; Lau, L. W.; Gerson, A. R.; Smart, R. S. C. *Appl. Surf. Sci.* **2011**, *257*, 2717-2730.

(47)   McCrory, C. C.; Jung, S.; Peters, J. C.; Jaramillo, T. F. *J. Am. Chem. Soc.* **2013**, *135*, 16977-16987.

(48)   Faber, M. S.; Dziedzic, R.; Lukowski, M. A.; Kaiser, N. S.; Ding, Q.; Jin, S. *J. Am. Chem. Soc.* **2014**, *136*, 10053-10061.

(49)   Liang, H.; Gandi, A. N.; Xia, C.; Hedhili, M. N.; Anjum, D. H.; Schwingenschlögl, U.; Alshareef, H. N. *ACS Energy Lett.* **2017**, *2*, 1035-1042.

(50)   Tang, C.; Wang, H. S.; Wang, H. F.; Zhang, Q.; Tian, G. L.; Nie, J. Q.; Wei, F. *Adv.*

Mater. **2015**, *27*, 4516-4522.

(51)   Zhong, J.-H.; Wang, A.-L.; Li, G.-R.; Wang, J.-W.; Ou, Y.-N.; Tong, Y.-X. *J. Mater.*

Chem. **2012**, *22*, 5656-5665.

(52)   Jung, S.; McCrory, C. C.; Ferrer, I. M.; Peters, J. C.; Jaramillo, T. F. *J. Mater. Chem.*

A **2016**, *4*, 3068-3076.

(53)   Xu, R.; Wu, R.; Shi, Y.; Zhang, J.; Zhang, B. *Nano Energy* **2016**, *24*, 103-110.

Table of Contents Graphic